PHYSICAL REVIEW A **95**, 033413 (2017)

Enhancing high-order-harmonic generation by time delays between two-color, few-cycle pulses

Dian Peng (彭典),[1] Liang-Wen Pi (皮良文),[1] M. V. Frolov,[2,3] and Anthony F. Starace[1]
[1]*Department of Physics and Astronomy, University of Nebraska, Lincoln, Nebraska 68588-0299, USA*
[2]*Department of Physics, Voronezh State University, Voronezh 394006, Russia*
[3]*Institute of Applied Physics, Russian Academy of Sciences, Nizhny Novgorod 603950, Russia*

(Received 23 September 2016; published 16 March 2017)

Use of time delays in high-order-harmonic generation (HHG) driven by intense two-color, few-cycle pulses is investigated in order to determine means of optimizing HHG intensities and plateau cutoff energies. Based upon numerical solutions of the time-dependent Schrödinger equation for the H atom as well as analytical analyses, we show that introducing a time delay between the two-color, few-cycle pulses can result in an enhancement of the intensity of the HHG spectrum by an order of magnitude (or more) at the cost of a reduction in the HHG plateau cutoff energy. Results for both positive and negative time delays as well as various pulse carrier-envelope phases are investigated and discussed.

DOI: 10.1103/PhysRevA.95.033413

I. INTRODUCTION

Few-cycle laser pulses, due to their unique characteristics compared to conventional continuous-wave laser fields [1], have propelled advances in numerous areas. The short time duration (as short as femtoseconds) enables time-resolved studies of ultrafast processes in atoms and molecules in various pump-probe experiments [2–4]. A train of short pulses enables promising optical frequency comb and high-resolution laser spectroscopy [2,5]. Most important, high-intensity few-cycle pulses provide sufficient energy to drive highly nonlinear processes in gases, solids, or plasmas, such as the generation of high-order harmonics and attosecond pulses [1,4,6].

High-order-harmonic generation (HHG) is considered a promising means for producing a compact, table-top coherent light source [7,8]. The HHG process transforms available visible and near-infrared intense laser fields into ultrashort pulses that have frequencies in the extreme ultraviolet and x-ray regimes and pulse durations ranging from femtoseconds to attoseconds [9]. The rapidly developing field of attosecond physics, which is based upon HHG, has greatly advanced the investigation of ultrafast processes [8,10,11]. Moreover, the HHG spectra themselves are increasingly being utilized to probe or image molecular structures [4,10,12–14].

Although the physical process of HHG is mostly well understood [9,10,14–17], its low conversion efficiency remains a major limitation that prevents HHG from becoming an important new light source. Investigations of ways to address the low efficiency issue focus on two physical regimes that are important for HHG. On the macroscopic propagation level, reducing the phase mismatch through precise pressure tuning in gases or, alternatively, introducing very high gas pressures have become common practices in HHG experiments [1,18]. On the microscopic single-atom (or local cluster) interaction level, the use of two-color fields to enhance the intensities of harmonic spectra (such as by increasing ionization rates or by favoring short trajectories while suppressing long trajectories, etc.) has been investigated for more than two decades [19–26]. Recently, as a result of advances in optical technology, there has been renewed interest in HHG driven by two-color (or multicolor) laser pulses owing to the possibility of subcycle waveform control in the synthesis of such pulses [9,27]. Control of the synthesis of intense short pulses in turn allows the control of strong-field processes such as HHG [28,29]. Thus, e.g., a linear ramp with a dc offset has been proposed as “an optimum waveform which maximizes the electron recollision energy” [30,31]; a multicolor laser field of different polarizations has been employed to selectively enhance particular harmonics [32]; and studies have shown that synthesized two-color laser fields with favorable phase-matching conditions can enhance harmonic yields significantly [33–35].

In many of the investigations cited above, a time delay between two pulses is often treated as equivalent to a relative phase [or as an extra carrier-envelope phase (CEP)]. This phase-time delay equivalence is valid for long pulses: e.g., $\cos(\omega_1 t) + \cos(\omega_2 t + \phi) \equiv \cos(\omega_1 t) + \cos[\omega_2(t + \phi/\omega_2)]$, in which the phase ϕ is viewed as a time delay ϕ/ω_2 between the two pulses. However, as the pulses become shorter so that they have only a few oscillations, a time delay between two pulse envelopes can no longer be viewed as equivalent to a CEP shift (see, e.g., Fig. 10 in Ref. [36]). For two coherently superposed few-cycle pulses, it is more appropriate to consider the result as a single synthesized waveform [28,36]. Although it is well known that both time delays and CEPs play important roles in two-color few-cycle pulse synthesis, systematic investigations of the role that time delays play in HHG processes driven by two-color, few-cycle pulses have not to our knowledge yet been carried out.

In this paper, we study how the laser-pulse waveform resulting from a time delay between two component pulses affects the resulting HHG spectrum for the important cases of two-color, few-cycle pulses having carrier frequencies of either ω and 2ω or ω and 3ω. In general, we find that a higher field strength at the ionization of the active electron and a lower field strength during its acceleration and recombination lead to a higher HHG yield but lower cutoff energy than the opposite scenario (e.g., a lower field at ionization and a higher field during acceleration and recombination). Our results demonstrate the utility of using the time delay between two-color pulses as a sensitive means to control HHG spectra.

Our theoretical formulation and numerical methods for solving the time-dependent Schrödinger equation (TDSE) are presented briefly in Sec. II. Our numerical HHG spectra results for the H atom driven by two-color, few-cycle pulses differing by either a positive time delay (in which the harmonic pulse comes ahead of the fundamental pulse) or by a corresponding CEP shift [a no-time-delay (NTD) case for comparison with the time delay case] are presented in Sec. III. These TDSE numerical results, which show that the HHG spectra are highly sensitive to the introduction of a time delay between the two-color, few-cycle pulses, are analyzed and interpreted in Sec. IV by using both a time-frequency analysis and an analytic description of HHG driven by a short laser pulse [37–40]. These subcycle analyses of the electron dynamics reveal the underlying physics producing the different HHG spectra between the laser-pulse waveforms involving a time delay or not. The case of negative time delays is analyzed in Sec. V. Finally, a summary of our results and conclusions is presented in Sec. VI. Throughout this paper, unless otherwise specified, we employ atomic units ($m_e = \hbar = |e| = 1$).

II. THEORETICAL FORMULATION

Consider a two-color few-cycle pulse with NTD between its two component pulses, described by the following time-dependent vector potential:

$$A_{\mathrm{NTD}}(t) = -\frac{c}{\omega_1} f_1(t)\sin(\omega_1 t + \phi_1) - \frac{c}{\omega_2} f_2(t)\sin(\omega_2 t + \phi_2), \tag{1}$$

where ω_1 and ω_2 are the carrier frequencies of the two pulses, ϕ_1 and ϕ_2 are the CEPs, and $f_1(t)$ and $f_2(t)$ are the pulse envelopes (which we assume are time-even functions with maxima at $t = 0$). Compare this field to the sum of two laser pulses with a time delay (TD) τ:

$$A_{\mathrm{TD}}(t) = -\frac{c}{\omega_1} f_1(t)\sin(\omega_1 t + \phi_1) - \frac{c}{\omega_2} f_2(t+\tau)\sin[\omega_2(t+\tau) + \phi_2']. \tag{2}$$

In order to focus our investigation on the effect of shifting the position in time of the second pulse envelope, we compare the HHG spectrum produced by the time-delay field $A_{\mathrm{TD}}(t)$ with that produced by the no-time-delay field $A_{\mathrm{NTD}}(t)$ for the case in which the arguments of the sine functions of the second pulses in each of the two fields are the same, i.e., we require in general that

$$\omega_2\tau + \phi_2' = \phi_2. \tag{3}$$

More specific conditions ensuring the overlap of the two pulses and taking into account the 2π periodicity of the CEPs are discussed below; see Eqs. (8) and (28). Thus, the only difference between the fields $A_{\mathrm{NTD}}(t)$ and $A_{\mathrm{TD}}(t)$ is that the $A_{\mathrm{TD}}(t)$ field has a time shift τ between the envelope peaks of its two component pulses. Notice that a *positive delay* ($\tau > 0$) means the ω_2 pulse comes before the ω_1 pulse. The electric fields corresponding to the vector potentials $A_{\mathrm{NTD}}(t)$ and $A_{\mathrm{TD}}(t)$ in Eqs. (1) and (2) are applied to the hydrogen (H) atom and the HHG spectra are calculated and compared.

To calculate the HHG yield, we solve the TDSE for an H atom in a linearly polarized laser electric field $F(t)$ directed along the z axis within the dipole approximation and using the length gauge:

$$i\frac{\partial}{\partial t}\Psi(\boldsymbol{r},t) = \left[\frac{\boldsymbol{p}^2}{2} - \frac{1}{r} + zF(t)\right]\Psi(\boldsymbol{r},t). \tag{4}$$

The harmonic spectrum $S(\Omega)$ is then obtained from the Fourier transform of the time-dependent dipole acceleration $\ddot{D}_z(t)$ [41]:

$$S(\Omega) = \left|\frac{1}{t_f - t_i}\int_{t_i}^{t_f} dt\, \ddot{D}_z(t) e^{-i\Omega t}\right|^2, \tag{5}$$

where

$$\ddot{D}_z(t) \equiv \langle\Psi(\boldsymbol{r},t)| - \ddot{z}|\Psi(\boldsymbol{r},t)\rangle = \langle\Psi(\boldsymbol{r},t)|\frac{z}{r^3}|\Psi(\boldsymbol{r},t)\rangle + F(t). \tag{6}$$

The TDSE is solved in spherical coordinates using a time-dependent generalized pseudospectral method [42,43], in which the wave function is expanded in Legendre polynomials and the time propagation is done with a second-order split-operator technique.

In order to avoid any static field component of a short pulse [44,45], we derive the electric field $F(t)$ via the vector potential $A(t)$: $F(t) = -\partial_t A(t)/c$, where $A(t)$ is either $A_{\mathrm{TD}}(t)$ or $A_{\mathrm{NTD}}(t)$. In both our numerical and analytical calculations we employ pulse envelopes defined as follows:

$$f_i(t) = F_i e^{-2\ln 2\, t^2/\tau_i^2}\ (i = 1,2), \tag{7}$$

where F_i is the electric-field strength of the ith pulse component and τ_i is the full width at half maximum of the intensity profile of the ith component.

Since the goal of the present investigation is to determine how the time-delayed superposition of the two-color pulses in Eq. (2) forms a waveform $A_{\mathrm{TD}}(t)$ that enhances the intensity of the HHG spectrum relative to that produced by the waveform $A_{\mathrm{NTD}}(t)$ in Eq. (1), the two pulses in Eq. (2) must overlap (because otherwise one obtains the trivial HHG spectrum of two independent pulses). Moreover, in order that the peak field intensities of the waveform $A_{\mathrm{TD}}(t)$ are comparable to those of the waveform $A_{\mathrm{NTD}}(t)$, the magnitude of the TD τ must be kept small, i.e., $|\tau| < \tau_1/2$. It should be emphasized that the CEP dependence of the HHG yield is periodic in ϕ_2 with a period 2π [see Eq. (1)], while the TD dependence does not present such periodicity owing to the shift of the pulse envelope with the TD τ. For the case of $|\tau| < \tau_1/2$, the correspondence between ϕ_2 and τ in Eq. (3) can be refined by explicitly taking into account the 2π periodicity of the CEPs as follows:

$$\frac{\phi_2}{2\pi} = \frac{\tau}{T_2} + \frac{\phi_2'}{2\pi} - \left[\frac{\tau}{T_2} + \frac{\phi_2'}{2\pi}\right], \quad \tau > 0, \tag{8}$$

where $[x]$ is the integer part of x and $T_2 = 2\pi/\omega_2$. Note that τ_1 and τ_2 in Eq. (7) can be independently adjusted; we assume in this paper that $\tau_1 > \tau_2$ (as in the experiments of Ref. [28]).

III. NUMERICAL RESULTS: INTENSITY ENHANCEMENTS AND CUTOFF EXTENSIONS

We consider first a two-color field composed of a fundamental frequency and its second harmonic: $\lambda_1 = 2\pi c/\omega_1 = 1600$ nm and $\lambda_2 = 2\pi c/\omega_2 = 800$ nm. The two component

TABLE I. For the ω-2ω HHG results shown in Fig. 1, we give here the numerical values of the laser-pulse parameters in Eqs. (1) and (2) that are varied [ϕ_1, τ (in units of $T_2 = 2.67$ fs), and ϕ_2] as well as key measures of the corresponding HHG results (the cutoff energies $\Omega_c^{(\mathrm{TD})}$ (eV) and $\Omega_c^{(\mathrm{NTD})}$ (eV), the cutoff shifts $\Delta\Omega_c$ (eV) [see Eq. (9a)], and the intensity ratios R_c [see Eq. (9b)]).

Fig. 1	ϕ_1	τ (TD)	ϕ_2 (NTD)	$\Omega_c^{(\mathrm{TD})}$	$\Omega_c^{(\mathrm{NTD})}$	$\Delta\Omega_c$	R_c
(a)	0	$1.1T_2$ (2.9 fs)	0.2π	66.7	78.4	11.7	4.5
(b)	0	$1.45T_2$ (3.9 fs)	0.9π	53.1	54.3	1.2	3.3
(c)	0	$0.65T_2$ (1.7 fs)	1.3π	71.4	78.4	7.0	2.3
(d)	0	$0.8T_2$ (2.1 fs)	1.6π	75.5	86.4	10.9	4.6

pulses have comparable peak intensities, with 6×10^{13} W/cm^2 for ω_1 and 4×10^{13} W/cm^2 for ω_2. They both have short pulse durations: $\tau_1 = 8.0$ fs ($1.5\,T_1$) and $\tau_2 = 5.6$ fs ($2.1\,T_2$), where $T_i \equiv 2\pi/\omega_i$ is the period for each carrier frequency.

For clarity, we set $\phi_2' = 0$ for the TD field A_{TD} (see the end of this section for a brief discussion about cases when $\phi_2' \neq 0$). The CEP of the first pulse ϕ_1 is set equal to zero initially. We choose four time delays so that their corresponding phases cover the range $[0,2\pi]$. The values of the pairs of time delays and phases are shown in Table I. The HHG results of our TDSE calculations for these eight cases are shown in Fig. 1 in panels (a), (b), (c), and (d). In each of the panels of Fig. 1, we compare the HHG spectra produced by the laser fields $F_{\mathrm{NTD}}(t)$ and $F_{\mathrm{TD}}(t)$ corresponding to the vector potentials in Eqs. (1) and (2), respectively.

The results in Fig. 1 exhibit the expected behavior of HHG spectra produced by few-cycle pulses: the CEP dependence, the multiplateau structure, the large wavy oscillations (due to the subcycle interference of long and short trajectories) [46], and the fine scale oscillations (due to intercycle interference) [16,38,39]. Besides these common features, the two curves in each plot are rather different near the cutoff region, despite the similarity of their electric fields. Moreover, there is one key common difference in the second plateaus (the higher-energy ones) in each panel: the no-time-delay field F_{NTD} gives a spectrum with a higher cutoff energy, whereas the time-delayed field F_{TD} gives a higher HHG yield near the cutoff. To quantify the difference, we define the energy shift of the cutoff, $\Delta\Omega_c$, and the ratio of HHG yields at the cutoff, R_c, as follows:

$$\Delta\Omega_c \equiv \Omega_c^{(\mathrm{NTD})} - \Omega_c^{(\mathrm{TD})}, \tag{9a}$$

$$R_c \equiv S^{(\mathrm{TD})}\big(\Omega_c^{(\mathrm{TD})}\big)/S^{(\mathrm{NTD})}\big(\Omega_c^{(\mathrm{NTD})}\big), \tag{9b}$$

where $\Omega_c^{(\mathrm{TD})}$ and $\Omega_c^{(\mathrm{NTD})}$ are the cutoff energies. Table I lists the numerical values of $\Delta\Omega_c$ and R_c. One sees that the intensity ratio, R_c, is always greater than unity ($R_c > 1$), indicating that the time-delayed fields give higher HHG yields near the cutoff. One sees also that all the energy shifts, $\Delta\Omega_c$, are greater than zero ($\Delta\Omega_c > 0$), indicating that the no-time-delay fields give higher cutoff energies.

In experiments, the CEP of the first pulse may not equal zero. Thus, we have calculated results for three cases involving $\phi_1 \neq 0$. The same $\omega - 2\omega$ pulses are used as in Fig. 1 with three pairs of time delays and phases as listed in Table II (together with key measures of their corresponding HHG results). The HHG spectra are shown in Fig. 2. One sees that the intensity enhancement ($R_c > 1$) and the cutoff extension ($\Delta\Omega_c \geqslant 0$) features occur again for all three pairs of TD and NTD results. Note that in Fig. 2(c) the cutoff extension happens also for the plateau with higher cutoff energies: $\Omega_c^{(\mathrm{TD})} = 58.9$ eV, $\Omega_c^{(\mathrm{NTD})} = 75.8$ eV, and $\Delta\Omega_c = 16.9$ eV.

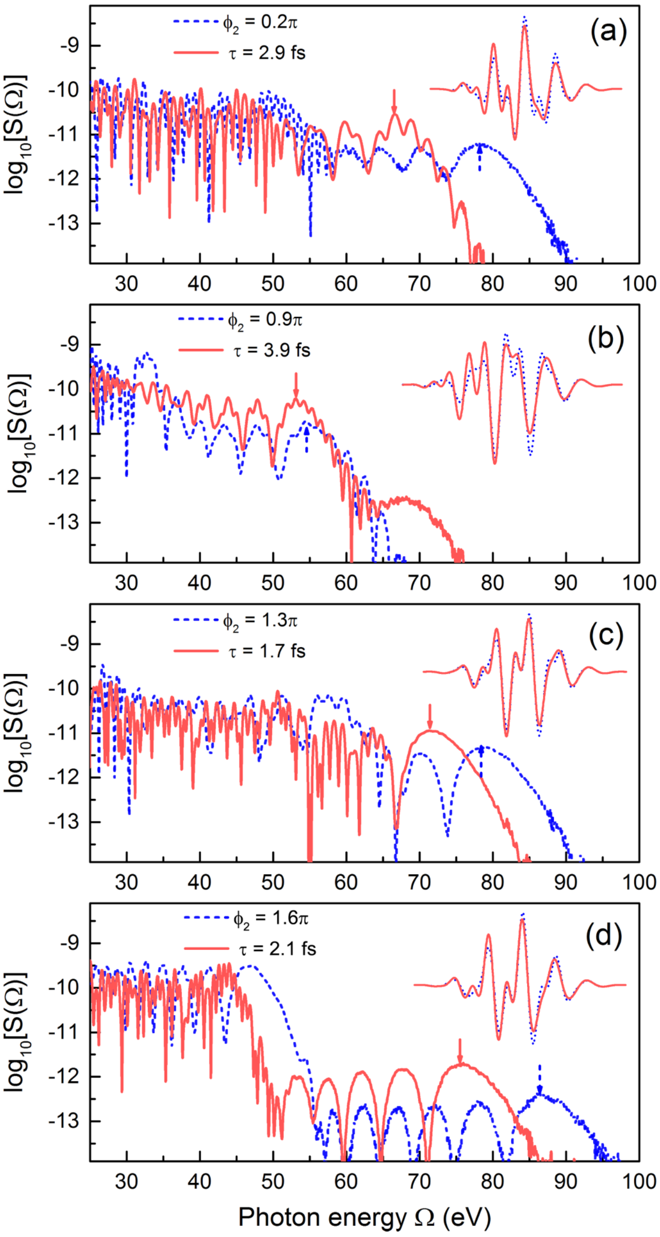

FIG. 1. Comparison of calculated two-color (ω-2ω) HHG spectra for the H atom produced by the linear combinations $A_{\mathrm{NTD}}(t)$ and $A_{\mathrm{TD}}(t)$ of 1600-nm (6×10^{13}W/cm^2, 8 fs) and 800-nm (4×10^{13}W/cm^2, 5.6 fs) pulses [see Eqs. (1) and (2)] for four different time delays τ and corresponding CEPs ϕ_2, with τ and ϕ_2 related according to Eq. (8). In each panel, the solid (red) line is for the TD case, and the dashed (blue) line is for the NTD case. In all panels, $\phi_1 = \phi_2' = 0$. The arrows indicate the locations of the cutoff energies, Ω_c, the values of which are given in Table I. The inset in each panel shows the electric fields $F_{\mathrm{NTD}}(t)$ and $F_{\mathrm{TD}}(t)$ corresponding to the vector potentials in Eqs. (1) and (2), respectively.

TABLE II. For the ω-2ω HHG results shown in Fig. 2, we give here the same laser-pulse parameters (for the case of $\phi_1 \neq 0$) and the same key measures of their HHG results as in Table I.

Fig. 2	ϕ_1	τ (TD)	ϕ_2 (NTD)	$\Omega_c^{(\mathrm{TD})}$	$\Omega_c^{(\mathrm{NTD})}$	$\Delta\Omega_c$	R_c
(a)	0.5π	$1.3T_2$ (3.5 fs)	0.6π	74.1	86.4	12.3	32.5
(b)	1.0π	$0.8T_2$ (2.1 fs)	1.6π	50.5	52.1	1.6	2.2
(c)	1.5π	$1.3T_2$ (3.5 fs)	0.6π	46.0	46.0	0.0	5.2

TABLE III. For the ω-3ω HHG results in Fig. 3, we give here the same laser-pulse parameters and the same key measures of the HHG results as in Table I. Note that $T_2' = 1.67$ fs.

Fig. 3	ϕ_1	τ (TD)	ϕ_2 (NTD)	$\Omega_c^{(\mathrm{TD})}$	$\Omega_c^{(\mathrm{NTD})}$	$\Delta\Omega_c$	R_c
(a)	0	$1.4T_2'$ (2.3 fs)	0.8π	51.3	58.5	7.2	61.2
(b)	0	$0.7T_2'$ (1.2 fs)	1.4π	62.8	69.0	6.2	4.5

We have also investigated ω-3ω two-color fields, since Jin *et al.* [33,34] proposed that "the third harmonic is the best in a two-color synthesis" of multicycle pulses when maximizing the HHG yield with a fixed cutoff energy. We have chosen a fundamental ω_1 with wavelength 1500 nm ($6 \times 10^{13}\,\mathrm{W/cm^2}$, 7.5 fs) and its third harmonic ω_2 with wavelength 500 nm ($4 \times 10^{13}\,\mathrm{W/cm^2}$, 3.5 fs). We have investigated two pairs of TD and NTD fields, the time delays and phases of which are listed in Table III. (Note that the CEP of the first pulse, ϕ_1, is again set equal to zero, and ϕ_2' is also zero.) The HHG results are shown in Fig. 3 and the cutoff energy shifts and intensity ratios, $\Delta\Omega_c$ and R_c, are given in Table III. As for the ω-2ω case in Fig. 1, the HHG results for the ω-3ω case display the same intensity enhancement and cutoff extension features: the time-delayed fields produce higher intensities near the cutoff at the cost of reduced cutoff energies as compared to the NTD fields.

Lastly, for the general case in which $\phi_2' \neq 0$, we have investigated cases over the range $\phi_2' \in [0,2\pi]$ in which ϕ_2 is held fixed and the time delay τ is varied [see Eqs. (3) and (8)]. Our calculations show that as τ increases, the HHG spectrum evolves as expected, i.e., the intensity enhancement and cutoff extension features increase in magnitude monotonically. Our calculations also show that when $\tau < 0.1\tau_1$, the HHG spectra for the TD and the NTD fields are nearly identical. As all of these results are as expected, we have not shown HHG spectra for cases in which $\phi_2' \neq 0$.

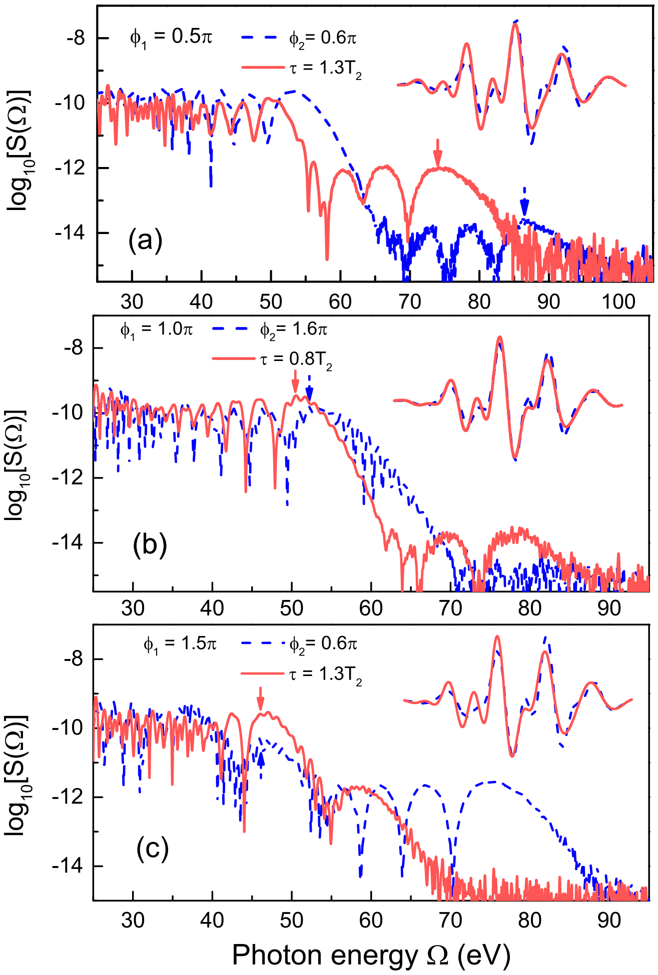

FIG. 2. Calculated HHG spectra for the H atom produced by the same two-color (ω-2ω) pulse as in Fig. 1 but with different time delays τ and CEPs ϕ_1 and ϕ_2. In each panel, the solid (red) line is for the TD case, and the dashed (blue) line is for the NTD case. For all TD pulses, $\phi_2' = 0$. The arrows indicate the locations of the cutoff energies, Ω_c, which are given in Table II. The inset in each plot shows the electric fields $F_{\mathrm{NTD}}(t)$ and $F_{\mathrm{TD}}(t)$ corresponding to the vector potentials in Eqs. (1) and (2), respectively.

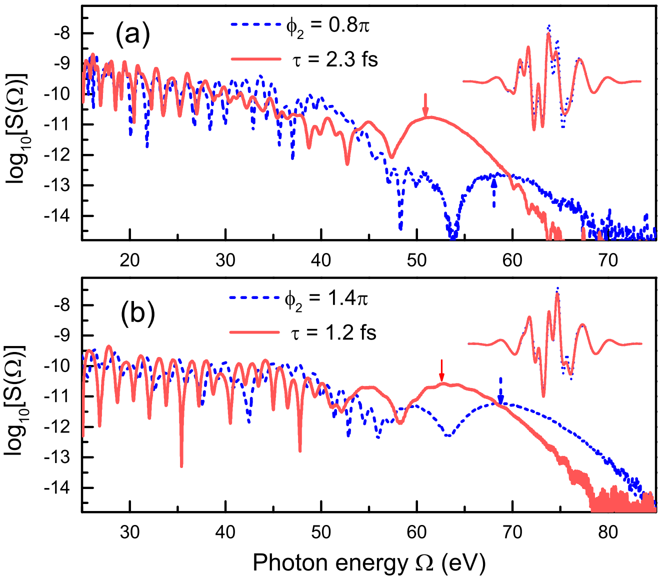

FIG. 3. Calculated two-color (ω-3ω) HHG spectra for the H atom produced by a linear combination of 1500-nm ($6 \times 10^{13}\,\mathrm{W/cm^2}$, 7.5 fs) and 500-nm ($4 \times 10^{13}\,\mathrm{W/cm^2}$, 3.5 fs) pulses with different phases and time delays. $\phi_1 = \phi_2' = 0$ for all panels. In each panel, the dashed (blue) line is for the NTD case, and the solid (red) line is for the TD case: (a) $\tau = 2.3$ fs, $\phi_2 = 0.8\pi$; (b) $\tau = 1.2$ fs, $\phi_2 = 1.4\pi$. The inset in each plot shows the electric fields $F_{\mathrm{NTD}}(t)$ and $F_{\mathrm{TD}}(t)$ corresponding to the vector potentials in Eqs. (1) and (2), respectively. The arrows indicate the locations of the cutoff energies, Ω_c, which are given in Table III.

IV. ANALYSIS AND INTERPRETATION OF THE RESULTS

In order to understand the physics behind the differences in the spectra in the time-delay and no-time-delay cases, specifically the intensity enhancement and cutoff extension features, we have employed both a time-frequency analysis and a closed-form analytic description of HHG spectra produced by few-cycle pulses [38–40] to interpret the results of our TDSE calculations.

To avoid repetition, we have selected for our analysis the HHG spectra shown in Fig. 1(d). The spectra show clearly that the TD field (with $\tau = 2.1$ fs) gives a higher HHG yield in the second (higher energy) plateau region, with an intensity ratio of $R_c = 4.6$ [see Eq. (9b)], whereas the NTD field (with $\phi_2 = 1.6\pi$) gives a higher cutoff, with an energy shift of $\Delta\Omega_c = 10.9$ eV.

A. Time-frequency analysis of the HHG spectra

We use the Gabor transform [47,48] for our time-frequency analysis: the dipole acceleration, $\ddot{D}_z(t)$ [Eq. (6)], is multiplied by a Gaussian window function before being Fourier transformed. Figures 4(a) and 4(b) plot our time-frequency analysis results for the TDSE calculations in Fig. 1(d), showing the correspondence between the recombination times and the harmonic energies.

One sees in Fig. 4 that there are clearly three main bursts of high harmonics, labeled as 1, 2, and 3 in the figure, which appear around times −2.5, 1.2, and 3 fs. The electric fields are also plotted in Fig. 4(c) for easier comparison. From the energy distribution, one can tell that it is the second burst that contributes to the second (higher energy) plateau in the spectrum. Comparing the two figures (a) and (b), one sees that the second burst in (a) leads to the generation of more energetic photons than the one in (b), but for the latter case the HHG yield is more intense, which explains qualitatively the origin of the differences in the spectra in Fig. 1(d).

B. Analytic analysis of the HHG spectra

For a more quantitative understanding of our results, we have employed an analytical description of HHG spectra produced by few-cycle pulses [38–40]. In this analytic description, the harmonic spectrum $\rho(\Omega)$ is obtained by coherently adding a handful of amplitudes corresponding to ionized electron trajectories (labeled by j and k) from different half cycles of the laser pulse:

$$\rho(\Omega) = \sum_{j,k} s_{jk} \cos(\varphi_j - \varphi_k)\mathcal{A}_j(E)\mathcal{A}_k(E), \tag{10}$$

where the harmonic photon energy Ω and the returning electron energy E satisfy the relation

$$\Omega = E + |E_0|. \tag{11}$$

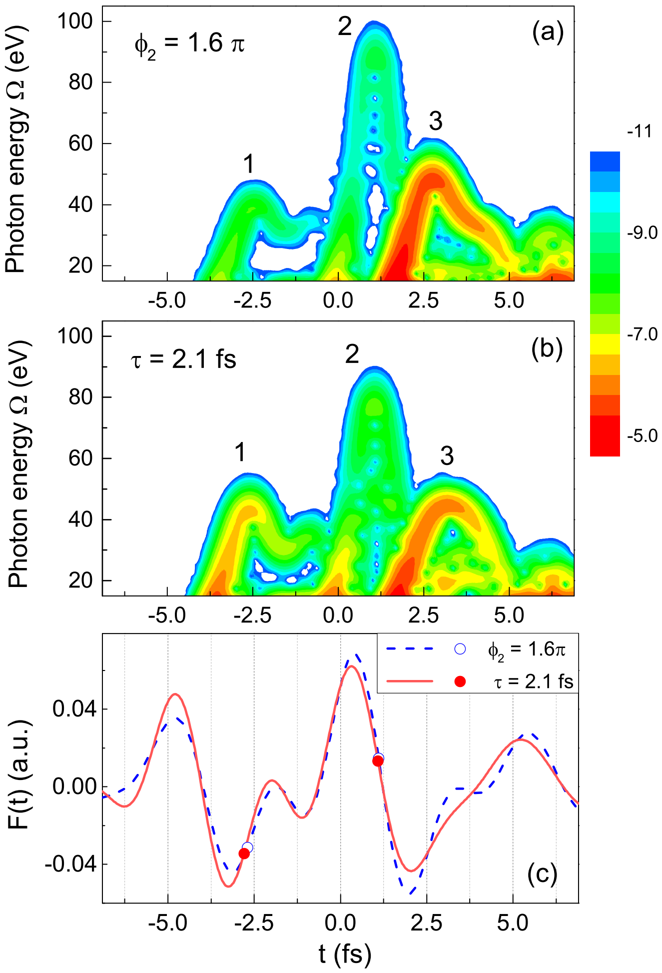

FIG. 4. Time-frequency analysis of the TDSE spectra in Fig. 1(d). (a) Time-frequency results for the laser electric field $F_{\rm NTD}(t)$ with $\phi = 1.6\pi$. (b) Time-frequency results for the laser electric field $F_{\rm TD}(t)$ with $\tau = 2.1$ fs. In both (a) and (b) the intensities of the spectra are plotted on a color-coded log scale shown at the right of the figure. (c) The electric fields $F_{\rm NTD}(t)$ and $F_{\rm TD}(t)$ [which correspond to the vector potentials in Eqs. (1) and (2), respectively, and are the same fields as in the inset in Fig. 1(d)] are plotted vs time on the same scale as in (a) and (b), and the dots are the ionization and recombination times of the second trajectory in Table IV.

Here E_0 is the ground-state energy of the electron, which equals $E_0 = -1/2$ for the hydrogen atom. [The sign factors $s_{jk} = \pm 1$ in Eq. (10) are defined in Eq. (26) below.] Each amplitude $\mathcal{A}_j(E)$ equals the square root of a product of three factors representing the three steps of high harmonic generation: the ionization factor $\mathcal{I}_j$, the propagation factor $\mathcal{W}_j(E)$, and the recombination factor $\sigma^{(r)}(E)$:

$$\mathcal{A}_j(E) \equiv \sqrt{\mathcal{I}_j \mathcal{W}_j(E)\sigma^{(r)}(E)}. \tag{12}$$

The calculation of each $\mathcal{A}_j(E)$ amplitude begins by noting that it corresponds to a classical trajectory that starts at $t_i^{(j)}$ (the ionization time), and ends at $t_r^{(j)}$ (the recombination time). These times satisfy equations for a closed trajectory along which an electron with zero initial velocity gains a maximum classical energy, $\mathcal{E}^{(\rm cl)}_{\rm max}(j)$:

$$\int_{t_i^{(j)}}^{t_r^{(j)}} A(t)dt - \left(t_r^{(j)} - t_i^{(j)}\right)A\left(t_i^{(j)}\right) = 0, \tag{13a}$$

$$A\left(t_r^{(j)}\right) - A\left(t_i^{(j)}\right) + cF\left(t_r^{(j)}\right)\left(t_r^{(j)} - t_i^{(j)}\right) = 0, \tag{13b}$$

where Eq. (13a) describes the closed trajectory (over which the electron returns to its starting point), and Eq. (13b) gives the maximum energy acquired by the electron [see Eq. (2) in Ref. [38]]. Here $A(t)$ is the vector potential and $F(t)$ is the laser electric field. The classical energy, $\mathcal{E}_{\max}^{(\mathrm{cl})}(j)$, is calculated in terms of the change in momentum:

$$\mathcal{E}_{\max}^{(\mathrm{cl})}(j) = \frac{1}{2c^2}\left[A\left(t_r^{(j)}\right) - A\left(t_i^{(j)}\right)\right]^2. \tag{14}$$

The phase, φ_j, of the jth amplitude is evaluated by integrating the classical action along the trajectory [see Eq. (55) in Ref. [39]]:

$$\varphi_j = \Omega t_r^{(j)} - \int_{t_i^{(j)}}^{t_r^{(j)}} \left\{\frac{1}{2c^2}\left[A(t) - A\left(t_i^{(j)}\right)\right]^2 - |E_0|\right\} dt. \tag{15}$$

The ionization factor for an electron in the 1s state of the H atom by laser-induced tunneling is [see Eq. (75) in Ref. [39]]

$$\begin{aligned} \mathcal{I}_j &= \frac{4}{\pi}\tilde{\gamma}_j^2 \Gamma_{st}(\tilde{F}_j), \\ \Gamma_{\mathrm{st}}(\tilde{F}_j) &= C_{10}^2 \frac{1}{\tilde{F}_j} e^{-\frac{2}{3\tilde{F}_j}}, \end{aligned} \tag{16}$$

where Γ_{st} is the tunneling rate for a bound atomic electron in a static electric field, and C_{10} is the coefficient of the electron's wave function at large (asymptotic) distances [see Eq. (26) in Ref. [39]]. For the 1s state in the H atom, $C_{10} = 2$. Also, $\tilde{F}_j$ is the magnitude of the electric field at the ionization time,

$$\tilde{F}_j = \left|F\left(t_i^{(j)}\right)\right|, \tag{17}$$

and the effective instantaneous Keldysh parameter $\tilde{\gamma}_j$ is defined as

$$\tilde{\gamma}_j \equiv \bar{\omega}\sqrt{2|E_0|}/\tilde{F}_j, \tag{18}$$

where $\bar{\omega} = \max(\omega_1, \omega_2)$. Combining Eqs. (16) and (18), the ionization factor can be written as

$$\mathcal{I}_j = \frac{16\bar{\omega}^2}{\pi}\frac{1}{\tilde{F}_j^3} e^{-2/(3\tilde{F}_j)}. \tag{19}$$

It is important to note that the intensity of the HHG spectrum is largely determined by the ionization factor, which is very sensitive to the strength of the electric field $\tilde{F}_j$ at the time of ionization.

The propagation factor $\mathcal{W}_j(E)$ is given by [see Eqs. (62)–(65), (70), and (72) in Ref. [39]]

$$\mathcal{W}_j(E) = \frac{\pi\Omega}{2\bar{\omega}^2}\sqrt{2E}\,\frac{\mathrm{Ai}^2(\xi_j)}{\Delta t_j^3 \zeta_j^{2/3}}, \tag{20}$$

where $\mathrm{Ai}(\xi)$ is the Airy function, and

$$\Delta t_j = t_r^{(j)} - t_i^{(j)}, \tag{21}$$

$$\xi_j = \frac{E - E_{\max}^{(j)}}{\zeta_j^{1/3}}, \tag{22}$$

$$E_{\max}^{(j)} = \mathcal{E}_{\max}^{(\mathrm{cl})}(j) - \frac{F\left(t_r^{(j)}\right)}{F\left(t_i^{(j)}\right)}|E_0|, \tag{23}$$

$$\zeta_j = \frac{F\left(t_r^{(j)}\right)^2}{2}\left[\frac{F\left(t_r^{(j)}\right)}{F\left(t_i^{(j)}\right)} - \frac{\dot{F}\left(t_r^{(j)}\right)}{F\left(t_r^{(j)}\right)}\Delta t_j - 1\right]. \tag{24}$$

The cutoff energy, $E_{\mathrm{cut}}^{(j)}$, of the HHG spectrum generated upon recombination of the electron traveling along the jth trajectory is encoded in the corresponding propagation factor and is largely determined by the electron's maximum classical energy, $\mathcal{E}_{\max}^{(\mathrm{cl})}(j)$, acquired along the jth trajectory [see Eq. (74) in Ref. [39]]:

$$E_{\mathrm{cut}}^{(j)} = |E_0| + \mathcal{E}_{\max}^{(\mathrm{cl})}(j) - \frac{F\left(t_r^{(j)}\right)}{F\left(t_i^{(j)}\right)}|E_0| - 1.019\zeta_j^{1/3}. \tag{25}$$

Note that the sign factors s_{jk} in the summation in Eq. (10) are determined by the signs of the Airy functions in Eq. (20):

$$s_{jk} = (-1)^{j-k}\,\mathrm{sign}[\mathrm{Ai}(\xi_j)\mathrm{Ai}(\xi_k)], \tag{26}$$

where $\mathrm{sign}[x] = +1(-1)$ if $x > 0(x < 0)$.

Finally, the recombination factor, $\sigma^{(r)}(E)$, is given by the photorecombination cross section of an electron to the 1s ground state of the H atom:

$$\begin{aligned} \sigma^{(r)}(E) &= 32\pi\alpha^3 \frac{\exp\left[-\frac{4}{p}\arctan(p)\right]}{p^2(1+p^2)^2(1-e^{-2\pi/p})}, \\ p &= \sqrt{2E}. \end{aligned} \tag{27}$$

Note that the energy dependence of the recombination factor depends only on the target and not on the laser field. Since our calculations are for the H atom in all cases, the recombination factor remains the same, and thus does not contribute to differences in the calculated HHG spectra.

Our analytic calculations for the HHG spectra are based upon Eq. (10). The calculations begin by solving Eqs. (13a) and (13b) for the ionized electron trajectories corresponding to the fields in Fig. 4(c), the electric-field amplitudes of which are $F_1 = 0.041$ a.u. and $F_2 = 0.034$ a.u. [see Eq. (7)]. Our calculations show that there are three major contributions to the HHG spectra (i.e., three trajectories with large ionization factors $\mathcal{I}_j$), one from each of three half cycles. For each of these three trajectories (for each field), we present the ionization and recombination times, the cutoff energies, the ionization factors, and the effective Keldysh parameters in Table IV. Results for the NTD field with $\phi_2 = 1.6\pi$ are presented in part (a) of Table IV, and results for the TD field with $\tau = 2.1$ fs are given in part (b). Notice that the three contributions for each field have a one-to-one correspondence with the three bursts shown in the time-frequency analysis results in Fig. 4: the jth contribution in Table IV(a) [or IV(b)] corresponds to the jth burst in Fig. 4(a) [or Fig. 4(b)]. For example, the third trajectory

TABLE IV. Numerical values of $t_i^{(j)}$ and $t_r^{(j)}$ [see Eqs. (13a) and (13b)], $E_{\rm cut}^{(j)}$ [see Eq. (25)], $\mathcal{I}_j$ [see Eq. (19)], and $\tilde{\gamma}_j$ [see Eq. (18)] for three half cycles of the pulses in Fig. 4(c). Part (a) is for the NTD field with $\phi_2 = 1.6\pi$, and part (b) is for the TD field with $\tau = 2.1$ fs.

j	$t_i^{(j)}$ (fs)	$t_r^{(j)}$ (fs)	$E_{\rm cut}^{(j)}$ (eV)	$\mathcal{I}_j$	$\tilde{\gamma}_j$
		(a)	$\phi_2 = 1.6\pi$		
1	−4.76	−2.34	38.6	2.37(−6)	1.6
2	−2.69	1.11	87.6	3.10(−7)	1.8
3	0.586	2.82	46.7	1.89(−3)	0.89
		(b)	$\tau = 2.1$ fs		
1	−4.71	−2.51	41.9	1.13(−4)	1.2
2	−2.80	1.09	75.6	1.68(−6)	1.6
3	0.476	3.31	43.7	1.10(−3)	0.95

for the NTD field in Table IV(a) has a return time of 2.8 fs, a cutoff energy of 46.7 eV, and the highest ionization factor, which all agree very well with the TDSE numerical results for burst 3 in our time-frequency analysis shown in Fig. 4(a).

The HHG spectra calculated analytically using Eq. (10) for three trajectories are shown in Fig. 5(a). The data for these three trajectories are given in Tables IV(a) and IV(b). For ease of comparison, the TDSE results in Fig. 1(d) are replotted in Fig. 5(b) on the same scale as in Fig. 5(a). Both the analytic and the TDSE HHG spectra have a two plateau structure and agree quantitatively on the cutoff energies of each plateau and qualitatively on the intensity enhancement features. The quantitative disagreement in the HHG intensities in the high-energy plateau region between the analytic and TDSE results is due to significant nontunneling ionization contributions to the TDSE results, as discussed in Sec. IV C below.

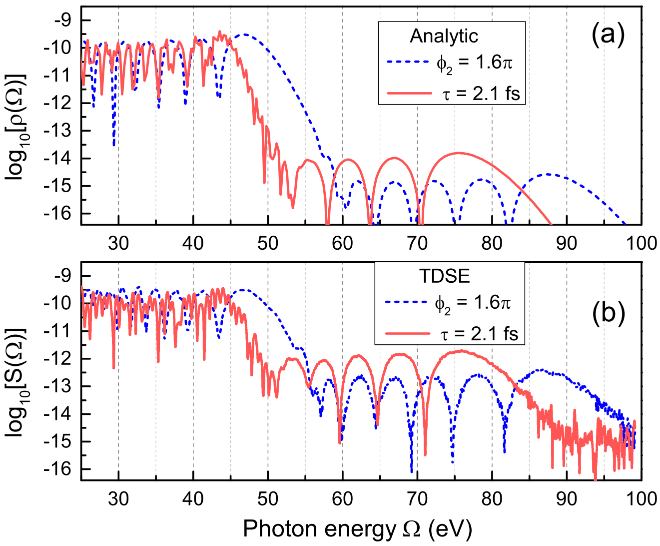

FIG. 5. Comparison of analytic and TDSE HHG spectra for the two laser fields shown in Fig. 4(c). (a) Analytic HHG spectra calculated from Eq. (10) are multiplied by a constant factor of 27.6 so that the low-energy plateau has the same intensity as the TDSE results. (b) TDSE HHG spectra calculated from Eq. (5) [which are the same results as in Fig. 1(d)].

In order to understand the cutoff energy and intensity differences in the analytic HHG spectra shown in Fig. 5(a) for the two fields shown in Fig. 4(c), we focus now on the contributions of the second trajectory ($j = 2$). This $j = 2$ trajectory, the data of which are given in Table IV and the ionization and recombination times of which are shown in Fig. 4(c), accounts for the higher-energy plateau in Fig. 5(a). At the time of ionization, the TD field has a larger amplitude than the NTD field, with a ratio of $F_{\rm TD}/F_{\rm NTD} = 1.1$. Since the ionization factor is very sensitive to the electric field [see Eq. (19)], this 10% greater amplitude for the TD field leads to a fivefold larger ionization factor, $\mathcal{I}_2^{(\rm TD)}/\mathcal{I}_2^{(\rm NTD)} = 5.4$, which explains the higher HHG yield in the spectrum produced by the TD field. The intensity ratio at the cutoff is $R_c = 5.9$ for the analytic results, and $R_c = 4.6$ for the TDSE results. To understand the difference in the cutoff energies, consider the recombination half cycle of the electric field in Fig. 4(c): the TD field has a smaller amplitude in the recombination half cycle and, hence, the returning electron gains less energy compared to its gain in the NTD field leading to a smaller cutoff energy. Our analytic calculations predict a cutoff energy difference for the two fields of $\Delta\Omega_c$= 12.0 eV, while our TDSE calculations predict a difference of $\Delta\Omega_c$= 10.9 eV.

Thus, our analytic analysis establishes a quantitative explanation for the different HHG spectra produced by our TDSE calculations for the TD and NTD two-color fields. Specifically, it explains the different cutoff energies and the intensity enhancement features in our TDSE results. A remaining question is the following: Why are the yields of the high-energy HHG plateau predicted by our analytic analysis far lower than those predicted by our TDSE results? We address this question in the next section.

C. Applicability of the analytic description

First, the analytic description is applicable in the tunneling regime, i.e., for instantaneous Keldysh parameters $\tilde{\gamma}_j < 1$. The lower intensity of the second (high energy) HHG plateau predicted by the analytic result [see Fig. 5(a)] as compared to the TDSE result [see Fig. 5(b)] is due to the fact that the relevant instantaneous Keldysh parameter, $\tilde{\gamma}_2$, is much larger than 1, as shown in Table IV. Our TDSE calculations, evidently, account for the ionization step exactly, taking into account all processes leading to ionization, while the analytic analysis, which is valid in the tunneling regime, only accounts for ionization by tunneling. Thus the TDSE results may be expected to produce higher HHG yields owing to the larger ionization rates in those calculations. Despite this violation of the assumptions of the analytic analysis, the analytic results still reproduce the cutoff extension and intensity enhancement features predicted by the TDSE calculations, which suggests that the other ionization mechanisms mainly affect the relative yields of the high-energy and low-energy HHG plateaus.

Second, the analytic analysis is valid for harmonics with energies close to the high-energy HHG plateau cutoff. Since the analytic HHG spectrum $\rho(\Omega)$ only includes trajectories with the maximum energies [see Eqs. (13a) and (13b)] in each half cycle, the HHG yields are in general less accurate for harmonics with energies far from the high-energy HHG cutoff. This explains the discrepancy in the shape of the second

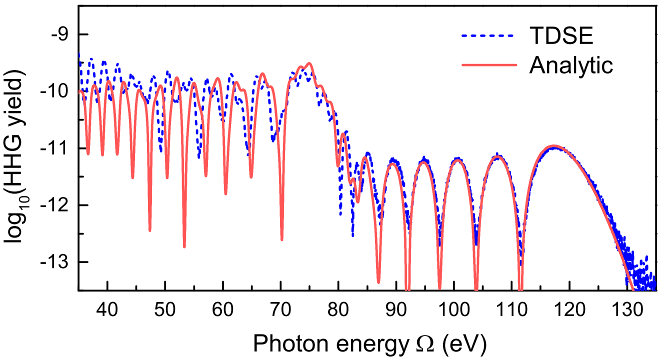

FIG. 6. Comparison of analytic and TDSE two-color HHG spectra for laser pulses of 1600 nm (1.2×10^{14} W/cm^2, 5.3 fs) and 800 nm (8×10^{13} W/cm^2, 3.8 fs) having no time delay with $\phi_1 = 0$ and $\phi_2 = 1.2\pi$. The solid (red) line is the analytic result, $\rho(\Omega)$, and the dashed (blue) line is the TDSE result, $S(\Omega)$. Note that $\rho(\Omega)$ is multiplied by an overall constant factor of 32.2.

(higher energy) plateau in Figs. 5(a) and 5(b) between 50 and 65 eV: namely, the energies of the oscillation minima in the TDSE results disagree increasingly from those in the analytic results as the energy decreases below the plateaus cutoffs.

In order to demonstrate the accuracy of the analytic analysis vis-a-vis the TDSE results, one must increase the field intensities (and/or use longer wavelengths) so that the instantaneous Keldysh parameter remains small for both plateaus. As an example, we have carried out HHG calculations for the following two-color laser fields: 1600 nm (1.2×10^{14} W/cm^2, 5.3 fs) and 800 nm (8×10^{13} W/cm^2, 3.8 fs) having no time delay with $\phi_1 = 0$ and $\phi_2 = 1.2\pi$. For these fields the instantaneous Keldysh parameter for the trajectory responsible for the low-energy HHG plateau is $\tilde{\gamma} = 0.83$, while that for the trajectory responsible for the high-energy plateau is $\tilde{\gamma} = 0.89$, i.e., both are now in the transitional regime ($\tilde{\gamma} < 1$), in which the tunneling ionization rates are reasonably accurate [49,50]. The corresponding analytic results are shown in Fig. 6 and compared with results of TDSE calculations. Except for an overall constant multiplicative factor, the analytic results are in extraordinarily good agreement with the TDSE calculation results for the HHG spectrum over a wide energy range from about 60 to 130 eV.

V. POSITIVE VERSUS NEGATIVE TIME DELAYS

So far, we have only considered the TD case in which the two component pulses of a two-color laser field have a positive time delay, $\tau > 0$, i.e., in which the harmonic pulse comes before the fundamental [see Eq. (2)]. In Sec. II the correspondence between a positive TD τ and a CEP ϕ_2 [for comparison with the NTD field in Eq. (1)] was given in Eq. (8). However, for a given CEP ϕ_2 ($0 \leqslant \phi_2 < 2\pi$) there is also a corresponding *negative* TD τ. By reasoning similar to that used in Sec. II for positive time delays, the correspondence between a negative TD τ and a NTD phase ϕ_2 is given by

$$\phi_2 = 2\pi\left(\frac{\tau}{T_2} - \left[\frac{\tau}{T_2}\right] + 1\right), \quad \tau < 0 \tag{28}$$

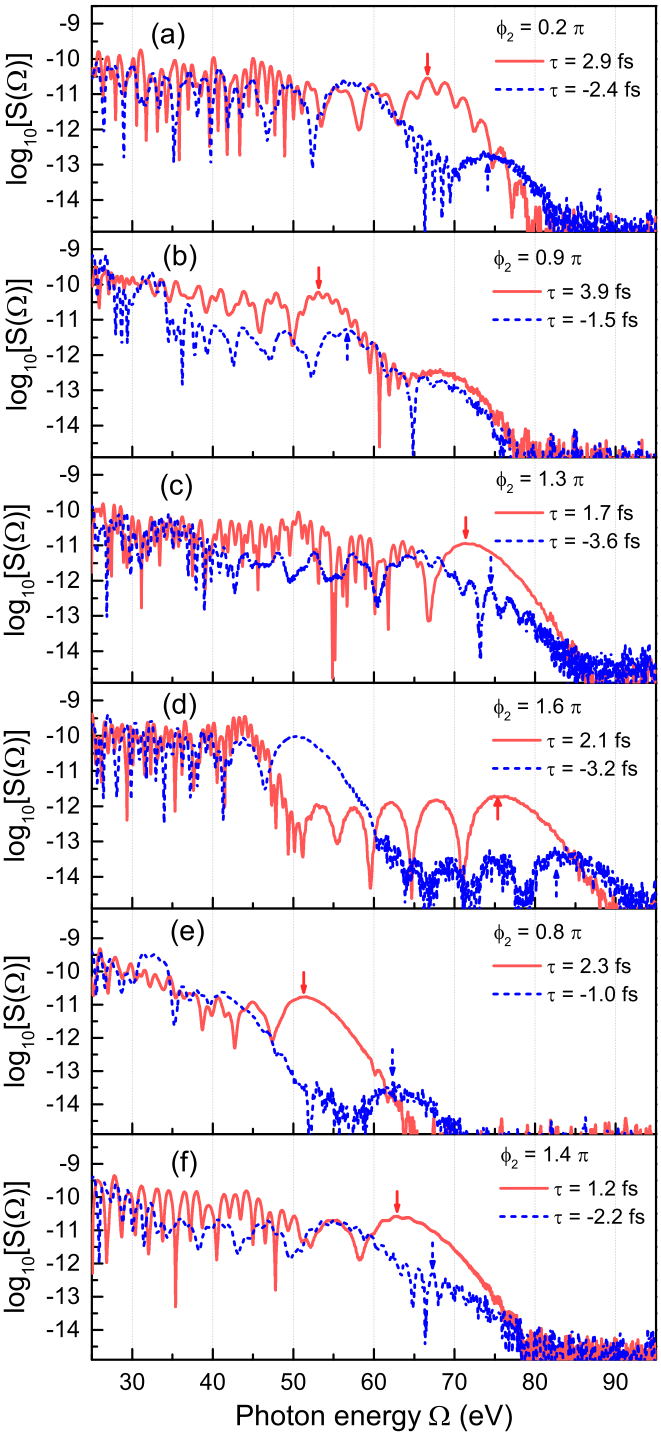

FIG. 7. Two-color HHG spectra predicted by TDSE calculations for laser pulses having positive (solid red line) and negative (dashed blue line) time delays. Results in panels (a)–(d) are for the same ω-2ω pulses as in Fig. 1; results in panels (e) and (f) are for the same ω-3ω pulses as in Fig. 3. Positive and negative time delays are calculated using, respectively, Eqs. (8) and (28). The arrows indicate the HHG plateau cutoff energies, the values of which are given in Table V.

where the extra "+1" has been added in order that the phase ϕ_2 remains in the range $[0,2\pi]$; also, we choose $\phi_2' = 0$. In this section, we present HHG spectra for pulses with negative time delays, in which the harmonic pulse comes after

TABLE V. Numerical values of the pairs of positive and negative time delays, τ, for a given ϕ_2 obtained from Eqs. (8) and (28). For each of the time delays, we give the cutoff energies, $\Omega_c^{(\mathrm{TD})}$ (eV), of the HHG spectra (shown in Fig. 7) that are produced by the corresponding TD fields [defined in Eq. (2), with $\phi_1 = \phi_2' = 0$]. See text for discussion.

Fig. 7	ϕ_2	τ (TD)	$\Omega_c^{(\mathrm{TD})}$
(a)	0.2π	$1.1T_2$ (2.9 fs)	66.7
		$-0.9T_2$ (-2.4 fs)	74.1
(b)	0.9π	$1.45T_2$ (3.9 fs)	53.1
		$-0.55T_2$ (-1.5 fs)	56.4
(c)	1.3π	$0.65T_2$ (1.7 fs)	71.4
		$-1.35T_2$ (-3.6 fs)	74.3
(d)	1.6π	$0.8T_2$ (2.1 fs)	75.1
		$-1.2T_2$ (-3.2 fs)	82.5
(e)	0.8π	$1.4T_2'$ (2.3 fs)	51.3
		$-0.6T_2'$ (-1.0 fs)	62.0
(f)	1.4π	$0.7T_2'$ (1.2 fs)	62.8
		$-1.3T_2'$ (-2.2 fs)	67.2

the fundamental, and compare the results with those for the positive time delay case, with both time delays corresponding to the same CEP ϕ_2.

The two-color HHG spectra predicted by our TDSE calculations are shown in Fig. 7 for the same ω and 2ω pulse parameters as in Fig. 1 and the same ω and 3ω pulse parameters as in Fig. 3; in all cases ϕ_1 and ϕ_2' are chosen equal to zero. Using Eqs. (8) and (28), we obtain for each chosen CEP ϕ_2 pairs of positive and negative TDs, the values of which are listed in Table V. In both Fig. 7 and Table V, (a)–(d) are for the $\omega - 2\omega$ case and (e) and (f) are for the $\omega - 3\omega$ case.

In each panel of Fig. 7 one sees that the negatively time-delayed pairs of pulses (in which the harmonic pulses come after the fundamental pulses) produce HHG spectra that have significantly lower intensities as compared to the positively time-delayed pairs of pulses (in which the harmonic pulses come before the fundamental pulses). The arrows in each panel of Fig. 7 indicate the HHG plateau cutoff energies, the values of which are given in Table V. One clearly sees that in each case the negative time-delay pulses produce HHG spectra with higher cutoff energies.

We have carried out both time-frequency and analytic analyses for the positive and negative time-delay TDSE results shown in Fig. 7(c). The time-frequency analyses of the positive and negative time-delay TDSE spectra in Fig. 7(c) are shown in Fig. 8. The numerical values of the analytic calculations for these two spectra are given in Table VI. Clearly, the harmonic bursts from the time-frequency analysis are in one-to-one correspondence with the half-cycle trajectory contributions in the analytical calculations.

Comparing the three harmonic bursts in Figs. 8(a) and 8(b), one sees that for the positive TD $\tau = 1.7$ fs all three bursts contribute to the harmonics with energies above 40 eV, whereas for the negative TD $\tau = -3.6$ fs only the first two bursts contribute to the higher-energy harmonics. These time-frequency results thus provide a qualitative explanation for the lower intensity of the HHG spectrum produced by the negative TD pulse in Fig. 7(c) (as compared to that for the positive TD pulse).

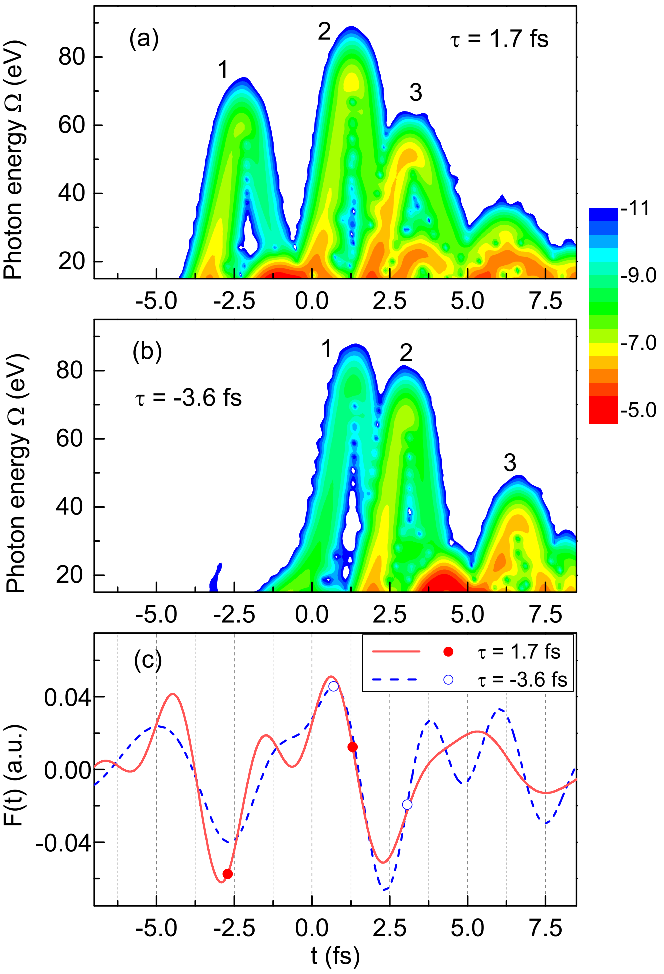

FIG. 8. Same as Fig. 4, but for the HHG spectra in Fig. 7(c).

The analytic analysis, the data of which are given in Table VI, provides a quantitative reason for the lower intensity of the HHG spectrum produced by the negative TD pulse. Comparing the trajectory contributions for the positive and negative TD pulses in Table VI, we see that the $j = 2$ contribution accounts for most of each spectrum in the high-energy region (40 eV and above) for both the positive and

TABLE VI. Numerical values of $t_i^{(j)}$ and $t_r^{(j)}$ [see Eqs. (13a) and (13b)], $E_{\mathrm{cut}}^{(j)}$ [see Eq. (25)], $\mathcal{I}_j$ [see Eq. (19)], and $\tilde{\gamma}_j$ [see Eq. (18)] for three half cycles of the pulses in Fig. 8(c). Part (a) is for $\tau = 1.7$ fs, and part (b) is for $\tau = -3.6$ fs. In each case, $\phi_2 = 1.3\pi$ [see Eq. (28)].

j	$t_i^{(j)}$ (fs)	$t_r^{(j)}$ (fs)	$E_{\mathrm{cut}}^{(j)}$ (eV)	$\mathcal{I}_j$	$\tilde{\gamma}_j$
		(a)	$\tau = 1.7$ fs		
1	-4.57	-2.19	59.3	1.97(-5)	1.4
2	-2.71	1.30	71.0	7.89(-4)	0.99
3	0.668	3.22	49.9	2.56(-4)	1.1
		(b)	$\tau = -3.6$ fs		
1	-2.54	1.36	74.4	1.27(-5)	1.4
2	0.690	3.06	66.0	7.93(-5)	1.2
3	2.63	6.67	34.2	8.77(-4)	0.98

negative TD pulses, judging from the ionization factors $\mathcal{I}_j$ and the cutoff energies $E_{\rm cut}^{(j)}$. The ionization and recombination times of the $j = 2$ trajectories are indicated by dots plotted on the curves for the laser fields in Fig. 8(c). These times are also given in Table VI. One sees that the electric field of the positive TD pulse has a larger magnitude at the time of ionization than that for the negative TD pulse. Thus it has a higher ionization factor, which leads to its having an HHG spectrum with a higher yield, as shown in Fig. 7(c).

VI. SUMMARY AND CONCLUSIONS

In this paper, we have investigated the HHG spectra produced by laser-pulse waveforms composed of time-delayed, two-color, few-cycle pulses using a TDSE method. Our focus has been on the time delay between the two pulse envelopes. We determine the effect of the TD τ on the HHG spectra by comparing the results with those produced by a superposition of similar pulses the envelopes of which are not separated in time, i.e., the NTD case. The component pulses in the NTD case are made similar to those in the TD case by introducing a phase ϕ_2 that is related to the time-delay τ according to Eqs. (8) and (28), depending, respectively, upon whether $\tau > 0$ or $\tau < 0$. Our results have shown that the TD waveform produced by the time-delayed two-color component pulses having $\tau > 0$ (in which the harmonic pulse comes before the fundamental frequency pulse) gives a higher-intensity HHG spectrum near the cutoff as compared to the NTD waveform. On the other hand, the NTD waveform gives a higher cutoff energy than does the TD waveform with $\tau > 0$. In all cases considered, the waveforms with $\tau > 0$ give orders of magnitude more intense HHG spectra than do those for $\tau < 0$. These intensity enhancement and cutoff extension features appear to be quite general: they are exhibited in the HHG spectra for both the $\omega - 2\omega$ and the $\omega - 3\omega$ two-color fields we have considered across a range of time delays and phases.

We have also elucidated the physical origin of these features using both time-frequency and analytic analyses of the HHG spectra produced by the pairs of few-cycle pulses. Specifically, for the cases we investigated, our analyses show that a positive time delay can produce a larger magnitude of the laser field in the half cycle in which ionization occurs and a lower magnitude of the laser field in the half cycle in which recombination occurs. A larger magnitude of the electric field at the time of ionization results in more ionized electrons and thus leads to a higher intensity of the HHG spectrum. On the other hand, a smaller magnitude of the electric field in the recombination half cycle results in a smaller energy gain of the returning electrons, and thus a lower cutoff energy.

To conclude, our paper has mapped out the time-delay features of two-color few-cycle pulses and has shown how time delays affect HHG spectra produced by such pulses for the H atom. The results of our investigations suggest that when using two-color few-cycle pulses to generate high harmonics, it is preferable to employ a positive time delay between the two pulses, i.e., the harmonic pulse should come before the fundamental in order to obtain higher HHG yields near the cutoff. On the other hand no time delay between the two pulses is preferred in order to obtain a higher HHG spectrum cutoff energy.

ACKNOWLEDGMENTS

Our TDSE and time-frequency analysis calculations were supported in part by NSF Grant No. PHYS-1505492 and were carried out at the Holland Computing Center of the University of Nebraska-Lincoln (UNL). A collaborative visit to UNL by M.V.F. and our analytic analyses were supported in part by NSF EPSCoR IRR Track II Research Award No. 1430519. The research of M.V.F. is supported in part by the Russian Science Foundation through Grant No. 15-12-10033.

---

[1] T. Brabec and F. Krausz, Intense few-cycle laser fields: Frontiers of nonlinear optics, Rev. Mod. Phys. **72**, 545 (2000).

[2] *Few-Cycle Laser Pulse Generation and its Applications*, edited by F. X. Kärtner (Springer-Verlag, Berlin, 2004).

[3] J.-C. Diels and W. Rudolph, *Ultrashort Laser Pulse Phenomena*, 2nd ed. (Academic, Burlington, 2006).

[4] S. Pabst, Atomic and molecular dynamics triggered by ultrashort light pulses on the atto- to picosecond time scale, Eur. Phys. J. Special Topics **221**, 1 (2013).

[5] *Femtosecond Optical Frequency Comb: Principle, Operation, and Applications*, edited by J. Ye and S. T. Cundiff (Springer, Boston, 2005).

[6] P. B. Corkum and F. Krausz, Attosecond science, Nat. Phys. **3**, 381 (2007).

[7] P. Agostini and L. F. DiMauro, The physics of attosecond light pulses, Rep. Prog. Phys. **67**, 813 (2004).

[8] *Ultrafast Dynamics Driven by Intense Light Pulses*, edited by M. Kitzler and S. Gräfe (Springer, Switzerland, 2016).

[9] M. C. Kohler, T. Pfeifer, K. Z. Hatsagortsyan, and C. H. Keitel, Frontiers of atomic high-harmonic generation (Chapter 4), Adv. At. Mol. Opt. Phys. **61**, 159 (2012).

[10] F. Krausz and M. Ivanov, Attosecond physics, Rev. Mod. Phys. **81**, 163 (2009).

[11] F. Calegari, G. Sansone, S. Stagira, C. Vozzi, and M. Nisoli, Topical Review: Advances in attosecond science, J. Phys. B **49**, 062001 (2016).

[12] J. Itatani, J. Levesque, D. Zeidler, H. Niikura, H. Pépin, J. C. Kieffer, P. B. Corkum, and D. M. Villeneuve, Tomographic imaging of molecular orbitals, Nature **432**, 867 (2004).

[13] X.-B. Bian and A. D. Bandrauk, Probing Nuclear Motion by Frequency Modulation of Molecular High-Order Harmonic Generation, Phys. Rev. Lett. **113**, 193901 (2014).

[14] A.-T. Le, H. Wei, C. Jin, and C. D. Lin, Tutorial: Strong-field approximation and its extension for high-order harmonic generation with mid-infrared lasers, J. Phys. B **49**, 053001 (2016).

[15] M. Lewenstein, Ph. Balcou, M. Yu. Ivanov, A. L'Huillier, and P. B. Corkum, Theory of high-harmonic generation by low-frequency laser fields, Phys. Rev. A **49**, 2117 (1994).

[16] A. de Bohan, P. Antoine, D. B. Milošević, and B. Piraux, Phase-Dependent Harmonic Emission with Ultrashort Laser Pulses, Phys. Rev. Lett. **81**, 1837 (1998).

[17] D. B. Milošević, D. Bauer, and W. Becker, Quantum-orbit theory of high-order atomic processes in intense laser fields, J. Mod. Opt. **53**, 125 (2006).

[18] T. Popmintchev, M.-C. Chen, D. Popmintchev, P. Arpin, S. Brown, S. Ališauskas, G. Andriukaitis, T. Balčiunas, O. D. Mücke, A. Pugzlys, A. Baltuška, B. Shim, S. E. Schrauth, A. Gaeta, C. Hernández-García, L. Plaja, A. Becker, A. Jaron-Becker, M. M. Murnane, and H. C. Kapteyn, Bright coherent ultrahigh harmonics in the keV X-ray regime from mid-infrared femtosecond lasers, Science **336**, 1287 (2012).

[19] S. Watanabe, K. Kondo, Y. Nabekawa, A. Sagisaka, and Y. Kobayashi, Two-Color Phase Control in Tunneling Ionization and Harmonic Generation by a Strong Laser Field and Its Third Harmonic, Phys. Rev. Lett. **73**, 2692 (1994).

[20] D. A. Telnov, J. Wang, and Shih-I Chu, Two-color phase control of high-order harmonic generation in intense laser fields, Phys. Rev. A **52**, 3988 (1995).

[21] A. D. Bandrauk, S. Chelkowski, H. Yu, and E. Constant, Enhanced harmonic generation in extended molecular systems by two-color excitation, Phys. Rev. A **56**, R2537 (1997).

[22] C. Figueira de Morisson Faria, D. B. Milošević, and G. G. Paulus, Phase-dependent effects in bichromatic high-order harmonic generation, Phys. Rev. A **61**, 063415 (2000).

[23] F. Ehlotzky, Atomic phenomena in bichromatic laser fields, Phys. Rep. **345**, 175 (2001).

[24] R. A. Ganeev, H. Singhal, P. A. Naik, I. A. Kulagin, P. V. Redkin, J. A. Chakera, M. Tayyab, R. A. Khan, and P. D. Gupta, Enhancement of high-order harmonic generation using a two-color pump in plasma plumes, Phys. Rev. A **80**, 033845 (2009).

[25] E. J. Takahashi, P. Lan, O. D. Mücke, Y. Nabekawa, and K. Midorikawa, Infrared Two-Color Multicycle Laser Field Synthesis for Generating an Intense Attosecond Pulse, Phys. Rev. Lett. **104**, 233901 (2010).

[26] K.-J. Yuan and A. D. Bandrauk, Invited Review: Circularly polarized attosecond pulses from molecular high-order harmonic generation by ultrashort intense bichromatic circularly and linearly polarized laser pulses, J. Phys. B **45**, 074001 (2012).

[27] C. Manzoni, O. D. Mücke, G. Cirmi, S. Fang, J. Moses, S.-W. Huang, K.-H. Hong, G. Cerullo, and F. X. Kärtner, Coherent pulse synthesis: Towards sub-cycle optical waveforms, Laser Photon. Rev. **9**, 129 (2015).

[28] S.-W. Huang, G. Cirmi, J. Moses, K.-H. Hong, S. Bhardwaj, J. R. Birge, L.-J. Chen, E. Li, B. J. Eggleton, G. Cerullo, and F. X. Kärtner, High-energy pulse synthesis with sub-cycle waveform control for strong-field physics, Nat. Photon. **5**, 475 (2011).

[29] A. Wirth, M. Th. Hassan, I. Grguraš, J. Gagnon, A. Moulet, T. T. Luu, S. Pabst, R. Santra, Z. A. Alahmed, A. M. Azzeer, V. S. Yakovlev, V. Pervak, F. Krausz, and E. Goulielmakis, Synthesized light transients, Science **334**, 195 (2011).

[30] L. E. Chipperfield, J. S. Robinson, J. W. G. Tisch, and J. P. Marangos, Ideal Waveform to Generate the Maximum Possible Electron Recollision Energy for Any Given Oscillation Period, Phys. Rev. Lett. **102**, 063003 (2009).

[31] S. Haessler, T. Balčiunas, G. Fan, G. Andriukaitis, A. Pugžlys, A. Baltuška, T. Witting, R. Squibb, A. Zaïr, J. W. G. Tisch, J. P. Marangos, and L. E. Chipperfield, Optimization of Quantum Trajectories Driven by Strong-Field Waveforms, Phys. Rev. X **4**, 021028 (2014).

[32] P. Wei, J. Miao, Z. Zeng, C. Li, X. Ge, R. Li, and Z. Xu, Selective Enhancement of a Single Harmonic Emission in a Driving Laser Field with Subcycle Waveform Control, Phys. Rev. Lett. **110**, 233903 (2013).

[33] C. Jin, G. Wang, H. Wei, A.-T. Le, and C. D. Lin, Waveforms for optimal sub-keV high-order harmonics with synthesized two- or three-colour laser fields, Nat. Commun. **5**, 4003 (2014).

[34] C. Jin, G. Wang, A.-T. Le, and C. D. Lin, Route to optimal generation of soft X-ray high harmonics with synthesized two-color laser pulses, Sci. Rep. **4**, 7067 (2014).

[35] C. Jin, G. J. Stein, K.-H. Hong, and C. D. Lin, Generation of Bright, Spatially Coherent Soft X-Ray High Harmonics in a Hollow Waveguide Using Two-Color Synthesized Laser Pulses, Phys. Rev. Lett. **115**, 043901 (2015).

[36] S.-W. Huang, G. Cirmi, J. Moses, K.-H. Hong, S. Bhardwaj, J. R. Birge, L.-J. Chen, I. V. Kabakova, E. Li, B. J. Eggleton, G. Cerullo, and F. X. Kärtner, Optical waveform synthesizer and its application to high-harmonic generation, J. Phys. B **45**, 074009 (2012).

[37] M. V. Frolov, N. L. Manakov, A. A. Silaev, and N. V. Vvedenskii, Analytic description of high-order harmonic generation by atoms in a two-color laser field, Phys. Rev. A **81**, 063407 (2010).

[38] M. V. Frolov, N. L. Manakov, A. A. Silaev, N. V. Vvedenskii, and A. F Starace, High-order harmonic generation by atoms in a few-cycle laser pulse: Carrier-envelope phase and many-electron effects, Phys. Rev. A **83**, 021405(R) (2011).

[39] M. V. Frolov, N. L. Manakov, A. M. Popov, O. V. Tikhonova, E. A. Volkova, A. A. Silaev, N. V. Vvedenskii, and A. F. Starace, Analytic theory of high-order-harmonic generation by an intense few-cycle laser pulse, Phys. Rev. A **85**, 033416 (2012).

[40] M. V. Frolov, N. L. Manakov, W.-H. Xiong, L.-Y. Peng, J. Burgdörfer, and A. F. Starace, Scaling laws for high-order-harmonic generation with midinfrared laser pulses, Phys. Rev. A **92**, 023409 (2015).

[41] A. D. Bandrauk, S. Chelkowski, D. J. Diestler, J. Manz, and K.-J. Yuan, Quantum simulation of high-order harmonic spectra of the hydrogen atom, Phys. Rev. A **79**, 023403 (2009).

[42] X.-M. Tong and Shih-I Chu, Theoretical study of multiple high-order harmonic generation by intense ultrashort pulsed laser fields: A new generalized pseudospectral time-dependent method, Chem. Phys. **217**, 119 (1997).

[43] D. A. Telnov and Shih-I Chu, Multiphoton detachment of H^- near the one-photon threshold: Exterior complex-scaling–generalized pseudospectral method for complex quasienergy resonances, Phys. Rev. A **59**, 2864 (1999).

[44] D. B. Milošević, G. G. Paulus, D. Bauer, and W. Becker, Topical Review: Above-threshold ionization by few-cycle pulses, J. Phys. B **39**, R203 (2006).

[45] A. D. Bandrauk, F. Fillion-Gourdeau, and E. Lorin, Tutorial: Atoms and molecules in intense laser fields: Gauge invariance of theory and models, J. Phys. B **46**, 153001 (2013).

[46] M. Yu. Kuchiev and V. N. Ostrovsky, Effective ATI channels in high harmonic generation, J. Phys. B **34**, 405 (2001).

[47] P. Antoine, B. Piraux, and A. Maquet, Time profile of harmonics generated by a single atom in a strong electromagnetic field, Phys. Rev. A **51**, R1750 (1995).

[48] R. Carmona, W.-L. Hwang, and B. Torrésani, *Practical Time-Frequency Analysis: Gabor and Wavelet Transforms with an Implementation in S* (Academic, San Diego, 1998).

[49] S. V. Popruzhenko, V. D. Mur, V. S. Popov, and D. Bauer, Strong Field Ionization Rate for Arbitrary Laser Frequencies, Phys. Rev. Lett. **101**, 193003 (2008).

[50] B. M. Karnakov, V. D. Mur, V. S. Popov, and S. V. Popruzhenko, Ionization of atoms and ions by intense laser radiation, JETP Lett. **93**, 238 (2011).